

Antiferromagnetic resonance in alkali-metal clusters in sodalite

Takehito Nakano,^{1,*} Hajime Tsugeno,² Atsufumi Hanazawa,¹ Takanari Kashiwagi,³ Yasuo Nozue,¹ and Masayuki Hagiwara²

¹*Department of Physics, Graduate School of Science, Osaka University, Toyonaka, Osaka 560-0043, Japan*

²*KYOKUGEN (Center for Quantum Science and Technology under Extreme Conditions), Osaka University, Toyonaka, Osaka 560-8531, Japan*

³*Institute of Materials Science and Graduate School of Pure and Applied Science, University of Tsukuba, Ibaraki 305-8573, Japan*

(Received 17 June 2013; revised manuscript received 17 October 2013; published 4 November 2013)

We have performed electron spin resonance (ESR) studies of K_4^{3+} and $(K_3Rb)^{3+}$ nanoclusters incorporated in powder specimens of aluminosilicate sodalite at several microwave frequencies between 9 and 34 GHz. The K_4^{3+} and $(K_3Rb)^{3+}$ clusters are arrayed in a bcc structure and are known to show antiferromagnetic ordering below the Néel temperatures of $T_N \simeq 72$ and $\simeq 80$ K, respectively, due to the exchange coupling between s electrons confined in the clusters. We have found sudden broadenings of ESR spectra in both samples below T_N . The line shape of the spectra below T_N is analyzed by powder pattern simulations of antiferromagnetic resonance (AFMR) spectra. The calculated line shapes well reproduce the experimental ones at all the frequencies by assuming a biaxial magnetic anisotropy. We have evaluated extremely small anisotropy fields of approximately 1 Oe indicating that these materials are ideal Heisenberg antiferromagnets. We have also found that the magnetic anisotropy changes from easy-plane type to uniaxial type by changing into a heavier alkali-metal cluster and that the g value shifts to a large value beyond two below T_N for K_4^{3+} and $(K_3Rb)^{3+}$ nanoclusters. These novel features of K_4^{3+} and $(K_3Rb)^{3+}$ nanoclusters incorporated in sodalite are discussed.

DOI: [10.1103/PhysRevB.88.174401](https://doi.org/10.1103/PhysRevB.88.174401)

PACS number(s): 76.50.+g, 75.30.Gw, 71.20.Dg, 82.75.Vx

I. INTRODUCTION

Zeolites are porous aluminosilicate crystals possessing regularly arrayed nanopores, such as “cages,” with rich varieties of structure. Alkali-metal clusters can be formed in the nanopores by loading guest alkali atoms, where s electrons are shared by several cations and confined in the cage. Exchange coupling between the s electrons in arrayed clusters realizes various kinds of magnetic orderings when the clusters have magnetic moments, such as ferromagnetism, antiferromagnetism, and ferrimagnetism, depending on the zeolite structure as well as the species of alkali element.^{1–6} These materials are in a new class of magnet because the magnetic orderings are realized by s electrons without any magnetic elements such as transition metals. In the present work, we aimed at one of the simplest systems among these materials, which are alkali-metal clusters incorporated in sodalite crystal. We have investigated the alkali-element dependence of the antiferromagnetic (AFM) properties in detail, especially on the magnetic anisotropy, of this material by multifrequency electron spin resonance (ESR) technique.

Sodalite is a kind of aluminosilicate zeolites possessing the simplest structure among zeolite family. The framework is built of oxygen-sharing AlO_4 and SiO_4 tetrahedra, and β cages with a truncated octahedron shape are arrayed in a bcc structure as shown in Fig. 1(a). This framework structure is classified as SOD type by IUPAC. The lattice constant is approximately 9 Å, which slightly varies depending on the species of alkali cations distributed in the cage. The β cage has an inside diameter of approximately 7 Å. The framework ($Al_3Si_3O_{12}$) is negatively charged, and four Na^+ cations, one monovalent anion X^- , e.g., Cl^- , OH^- and so on, and water molecules are accommodated in the β cage in an as-synthesized sodalite, resulting in a chemical formula of $Na_4XAl_3Si_3O_{12} \cdot xH_2O$. After removing the NaX salt and the water molecules, and expose it to sodium vapor, one Na atom can be adsorbed in the β cage and a

paramagnetic Na_4^{3+} cluster is formed.⁷ In this cluster, one s electron provided by the guest Na atom is shared by four Na^+ cations and confined in the β cage as schematically shown in Fig. 1(b). Srdanov and coworkers succeeded in preparing Na_4^{3+} clusters in almost all the β cages with a chemical formula of $Na_4Al_3Si_3O_{12}$ and found an AFM order below the Néel temperature $T_N \simeq 48$ K.³ The AFM phase transition has been confirmed by several techniques such as NMR,⁸ muon spin rotation (μ SR),⁹ antiferromagnetic resonance (AFMR),^{10,11} and neutron diffraction.¹² In the AFM state, the s -electron spins in the body centers are aligned antiparallel to those in the corners in the bcc lattice.¹² The temperature dependence of a local field detected by μ SR was well explained by a three-dimensional Heisenberg model with a cubic symmetry.⁹ AFMR studies also confirmed that this system is an ideal Heisenberg-type antiferromagnet, but a very weak magnetic anisotropy with the order of 1 Oe was found.^{10,11} Other alkali cations can be substituted for the Na^+ ions. K_4^{3+} clusters were also found to show AFM order at $T_N \simeq 72$ K.^{13–16} K-Rb alloy clusters of $(K_3Rb)^{3+}$ were also prepared and T_N was found to be $\simeq 80$ K.^{15,17} These materials are assigned to Mott insulators under a just-half-filled condition of s -like band of cluster array,^{18–22} where each cage accommodates one unpaired s electron. The systematic increase in T_N with increasing atomic weight of the alkali element has been well explained in the framework of Mott-Hubbard model as follows.^{15,21,22} Since the heavier alkali atom have a larger ion size and a shallower potential for electrons, the size of s -electron wave function of the cluster is expected to increase with increasing the atomic weight of alkali element. This leads to a decrease in U/t , where U is the on-site (on-cluster) Coulomb repulsion energy and t the electron transfer energy between adjacent clusters. Then, T_N increases as generally predicted in the Mott-Hubbard insulating phase.²³ Therefore the alkali-metal clusters in sodalite can be assigned to a prototype of

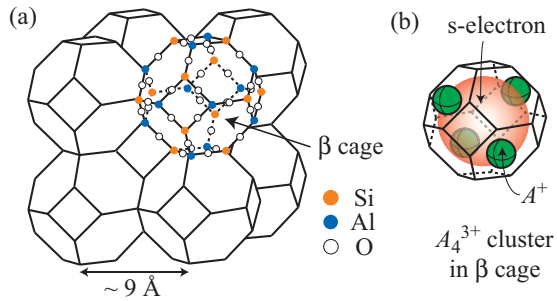


FIG. 1. (Color online) Schematic illustrations of (a) crystal structure of sodalite and (b) A_4^{3+} cluster formed in the β cage, where A is an alkali atom. The framework has the SOD-type structure with a bcc arrangement of the β cages.

Mott-Hubbard system in a cubic lattice. However, the origin of the weak magnetic anisotropy observed in Na_4^{3+} clusters has not been clarified.^{10,11} It is worth revealing much detailed properties of magnetism in these new materials, because it leads to a general and profound understanding of magnetism of the s -electron systems. In the present work, we performed ESR studies of K_4^{3+} and $(K_3Rb)^{3+}$ clusters in sodalite in order to investigate in detail the alkali-element dependence of the magnetic anisotropy in the AFM ordered phase.

II. EXPERIMENTAL PROCEDURE

The sample preparation method in the literatures^{13,15} was adopted in the present study. We used a powder specimen of Na-type sodalite crystal with a few micrometer size synthesized by Tosoh Corporation. We prepared a salt-free sodalite with a chemical formula of $Na_3Al_3Si_3O_{12}$ per β cage by washing with distilled water by means of the Soxhlet extraction method. A K-type sodalite with a chemical formula of $K_3Al_3Si_3O_{12}$ was prepared by the ion-exchange of the salt-free Na-type one in a KNO_3 aqueous solution. The K-type sodalite powder was then heated to 500 °C in a vacuum for 24 hours and fully dehydrated. Pure K and Rb metals were adsorbed into the dehydrated K-type sodalites with sealed in quartz glass tubes at 150 °C. In these samples, the chemical formulas are given by $K_4Al_3Si_3O_{12}$ and $K_3RbAl_3Si_3O_{12}$, respectively, and K_4^{3+} and $(K_3Rb)^{3+}$ clusters are generated in the respective β cages. The magnetic susceptibility was measured by a superconducting quantum interference device magnetometer (MPMS-XL, Quantum Design). We confirmed that the temperature dependence of the magnetic susceptibility was consistent with that in some reported works.^{14,15} We performed ESR measurements at frequencies between 9 and 34 GHz. At the X-band frequency (9 GHz), we used a conventional ESR apparatus (Bruker, EMX) and the temperature was controlled by a helium gas flow cryostat (Oxford Instruments). ESR signal was taken by sweeping a 100 kHz modulated external magnetic field with an amplitude of 1 Oe. The field-derivative spectra were integrated to obtain the absorption signals. At higher frequencies (20–34 GHz), we utilized a vector network analyzer MVNA (ABmm), a superconducting magnet (Oxford Instruments) and home-made ESR cylindrical resonators. The temperature was controlled by using a variable temperature

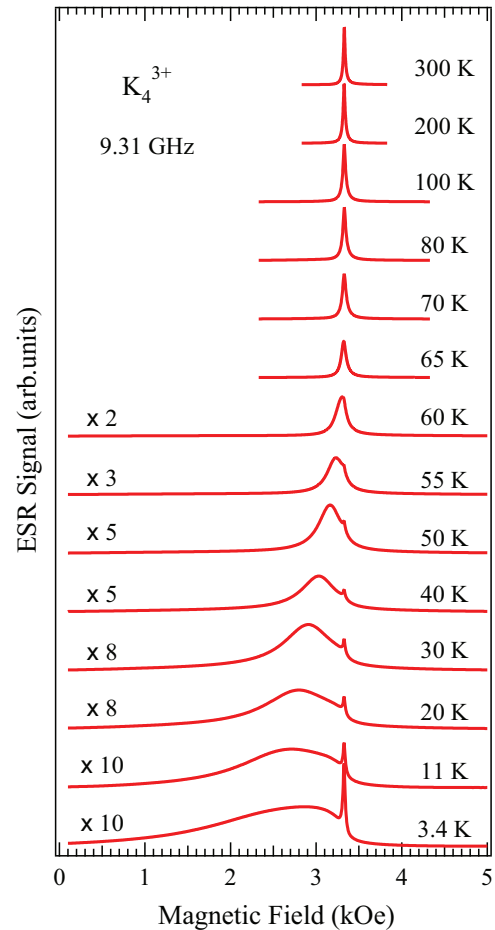


FIG. 2. (Color online) Temperature dependence of ESR spectra of K_4^{3+} clusters in sodalite measured at an X-band frequency, 9.31 GHz.

insert in the superconducting magnet and a manganine wire heater that was wound around the ESR resonators.

III. EXPERIMENTAL RESULTS

Figure 2 shows the temperature dependence of ESR spectra of K_4^{3+} clusters in sodalite measured at an X-band frequency, 9.31 GHz. At high temperatures, a signal with a Lorentzian line shape is observed. This is assigned to an exchange-narrowed paramagnetic resonance signal. The g -value is evaluated to be $g = 1.999$ at 300 K. Upon cooling, the linewidth increases and the spectral centroid systematically shifts to the low-field side. The line shape also significantly changes especially for the data below 65 K. As seen clearly in the lowest-temperature data, the spectral shape is asymmetric with a long tail on the low-field side. A sharp peak is also observed at 3.33 kOe. The integrated intensity of this sharp component is evaluated to be only 4% of the total integrated intensity. Figure 3 shows the temperature dependence of ESR spectra of $(K_3Rb)^{3+}$ clusters measured at 9.29 GHz. Overall features of the spectra seem similar to those in K_4^{3+} clusters, but there are discernible differences between two samples. In a paramagnetic state at high temperature, e.g., 300 K, the linewidth in $(K_3Rb)^{3+}$ clusters is much wider than that in K_4^{3+} clusters. The g value is evaluated to be $g = 1.994$, which is lower than that in K_4^{3+} clusters. Moreover,

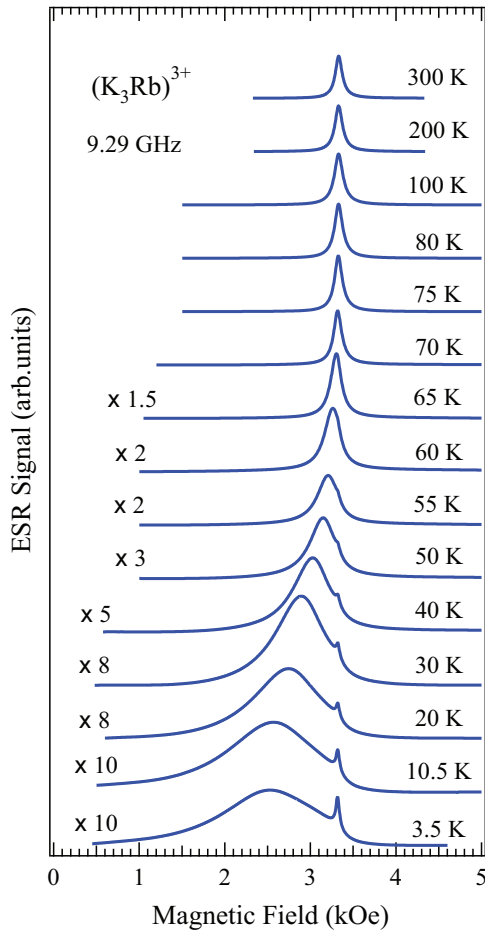


FIG. 3. (Color online) Temperature dependence of ESR spectra of $(\text{K}_3\text{Rb})^{3+}$ clusters in sodalite measured at X-band frequency, 9.29 GHz.

the spectral shape at low temperature is different from that in K_4^{3+} . The spectrum of $(\text{K}_3\text{Rb})^{3+}$ clusters is more symmetric and the centroid is at lower field than that in K_4^{3+} clusters. The low-temperature spectra of $(\text{K}_3\text{Rb})^{3+}$ also contain a small sharp peak at 3.32 kOe. The integrated intensity of this sharp component is only 2% of the total integrated intensity.

We estimated the full width at the half maximum (FWHM) of the spectra with neglecting the small sharp peak observed at low temperatures. They are plotted as a function of temperature in Fig. 4 together with that of Na_4^{3+} clusters.¹⁰ As reported in Ref. 10, the ESR linewidth of Na_4^{3+} clusters suddenly increases below $T_N \simeq 50$ K. The broad signal at low temperature was well explained by a powder pattern of AFMR signal. The FWHM of K_4^{3+} clusters shows similar behavior. In the high-temperature region, namely, in the paramagnetic state, the FWHM is slightly wider than that of Na_4^{3+} clusters. Upon cooling, the FWHM gradually increases, and then, rapidly increases below approximately 70 K, which coincides well with T_N . At the lowest temperature, the FWHM of K_4^{3+} clusters is more than twice as wide as that of Na_4^{3+} ones. On the other hand, in $(\text{K}_3\text{Rb})^{3+}$ clusters, the FWHM is approximately four times wider than that in K_4^{3+} clusters at high temperature. The FWHM shows a slight dip at about 75–80 K, and then, suddenly increases at low temperature. This also coincides

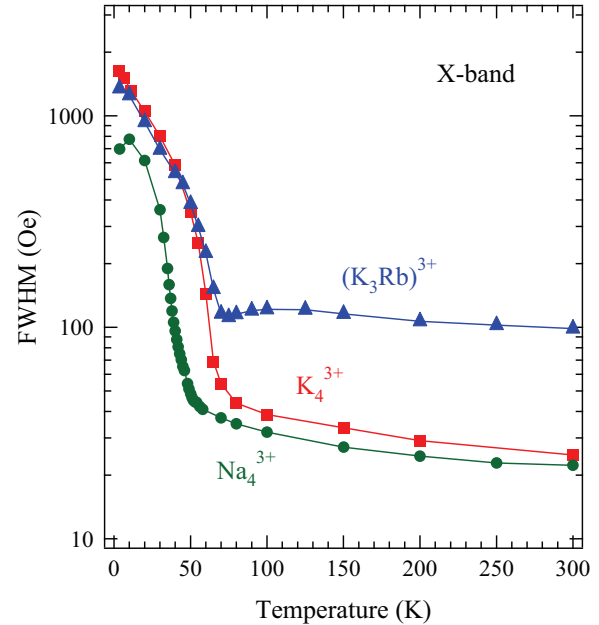


FIG. 4. (Color online) Temperature dependence of the ESR linewidth (FWHM) for Na_4^{3+} , K_4^{3+} and $(\text{K}_3\text{Rb})^{3+}$ clusters in sodalite measured at X-band frequency. The width is plotted on a logarithmic scale. The data for Na_4^{3+} clusters are taken from Ref. 10.

with T_N . The FWHM at the lowest temperature is nearly the same as that of K_4^{3+} clusters. These results clearly indicate that the line broadening arises from AFM ordering, because the broadening starts at the respective T_N both in K_4^{3+} and $(\text{K}_3\text{Rb})^{3+}$ clusters. Therefore the observed broad spectra at low temperature can be assigned to the powder patterns of AFMR signals on the analogy of Na_4^{3+} clusters.¹⁰ On the other hand, the sharp peaks at $\simeq 3.3$ kOe may be due to a paramagnetic signal from the isolated electrons in an incompletely loaded part of the sample or some magnetic impurities, because this component has a very weak intensity and behaves independently from the AFM phase transition. Such a tiny paramagnetic component was observed also in the magnetic susceptibility.^{3,9,10,15}

In order to compare the spectral shape in the antiferromagnetically ordered state in detail, the lowest-temperature data for all the samples are plotted in Fig. 5. The short vertical bars indicate a resonance field for $g = 2$ at each frequency. It is clear that the spectral shape systematically changes depending on the species of the alkali element. In Na_4^{3+} clusters, the spectrum has a long tail on the low-field side but drops sharply on the high-field side near the $g = 2$ position.¹⁰ In K_4^{3+} clusters, the spectrum is broadened and the peak position of the broad component significantly shifts to the low-field side. The shape is still asymmetric. In $(\text{K}_3\text{Rb})^{3+}$ clusters, the linewidth is similar to that of K_4^{3+} , but the peak position shifts to much lower field, resulting in the nearly symmetric shape.

We performed ESR measurements also at several frequencies up to 34 GHz at liquid helium temperatures. The results for K_4^{3+} and $(\text{K}_3\text{Rb})^{3+}$ clusters are shown in the upper and lower panels in Fig. 6, respectively. The black open circles with a solid line indicate the experimental data. The red solid curves and the blue dashed curves are the results of simulations as

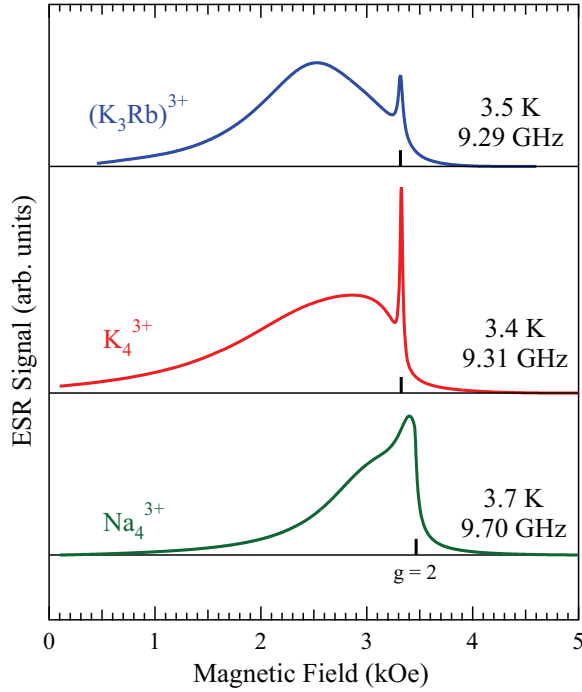


FIG. 5. (Color online) ESR spectra for Na_4^{3+} , K_4^{3+} and $(\text{K}_3\text{Rb})^{3+}$ clusters in sodalite measured at designated temperatures and at X-band frequencies. The data for Na_4^{3+} clusters are from Ref. 10. The short vertical bars indicate resonance fields at $g = 2$ for each frequency.

described later. In both samples, the spectrum is systematically shifted to a higher field and narrowed with increasing the microwave frequency. These are typical features in a powder pattern of AFMR signal. At the high frequency limit, all the AFMR branches converge to the electron paramagnetic resonance (EPR) branch as described in the next section. Thus, in the AFMR powder pattern at a high frequency, the peak position of the spectrum almost coincides with the EPR line. We evaluated the g values directly from the peak position of the spectra. The obtained values are $g = 2.048$ for K_4^{3+} clusters at 34.0 GHz and $g = 2.061$ for $(\text{K}_3\text{Rb})^{3+}$ clusters at 33.8 GHz. The values are significantly larger than those obtained at room temperatures. The large positive g shifts at low temperatures are obtained also in detailed analysis of the spectra as described in the next section.

IV. ANALYSIS

Generally, the frequency dependence of AFMR fields depends on the type of magnetic anisotropy, and several branches of the resonance modes appear. A powder pattern of AFMR signal is given by integrating the resonance lines over whole field directions to the crystal. Therefore the shape of the powder pattern strongly depends on the type of magnetic anisotropy. In the case of Na_4^{3+} clusters in sodalite, the observed ESR signal was well reproduced by an AFMR powder pattern with an easy-plane-type anisotropy as reported in the previous works including a multi-frequency ESR study.^{10,11} In the case of easy-plane-type anisotropy, there are two modes with the resonance conditions of $\omega_{\parallel}/\gamma = H$

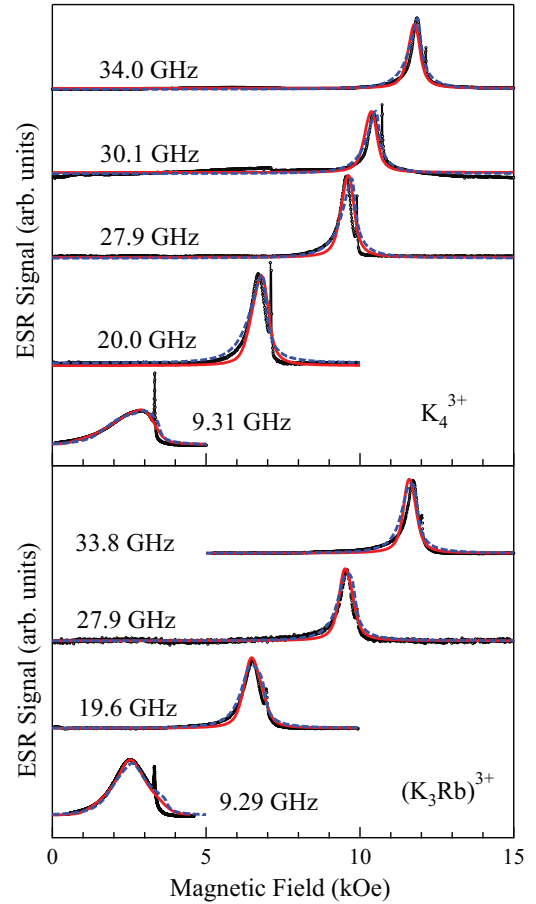


FIG. 6. (Color online) ESR spectra for K_4^{3+} and $(\text{K}_3\text{Rb})^{3+}$ clusters in sodalite measured at liquid helium temperatures at several frequencies. The black open circles with a solid line show the experimental data. The red solid curves and the blue dashed curves are the simulation results of the AFMR powder pattern by assuming an isotropic and an anisotropic relaxation processes, respectively.

and $\omega_{\perp}/\gamma = \sqrt{H^2 + 2H_E H_A}$ under an applied external magnetic field H parallel and perpendicular to the easy plane, respectively. ω_{\parallel} and ω_{\perp} are the resonant angular frequencies, γ the gyromagnetic ratio of electron spin, H_E the exchange field, and H_A the anisotropy field. The exchange field is given by

$$H_E = 2z_1 |J_1| s / g\mu_B, \quad (1)$$

where J_1 indicates the exchange coupling constant between the nearest neighbors (NNs) in the Heisenberg Hamiltonian $\mathcal{H} = 2J_1 \sum_{NN} \mathbf{S}_i \cdot \mathbf{S}_j$, and z_1 the number of NNs. Since there is no resonance mode at fields higher than the doubly degenerated $\omega_{\parallel}/\gamma = H$ mode, the powder pattern exhibits an asymmetric shape with a long tail on the low-field side and a sharp drop on the high-field side. This feature of the line shape coincides well with the spectrum of Na_4^{3+} clusters in sodalite.^{10,11} On the other hand, the observed spectra of K_4^{3+} and $(\text{K}_3\text{Rb})^{3+}$ clusters have a fairly long tail also on the high-field side as seen in Fig. 5. Thus we could not reproduce the spectra by assuming an easy-plane-type anisotropy. Then, we tried to reproduce the spectra by assuming a uniaxial and a biaxial magnetic anisotropies, and the latter of which was found to give the best fit. The powder pattern simulation was performed in the following manner.

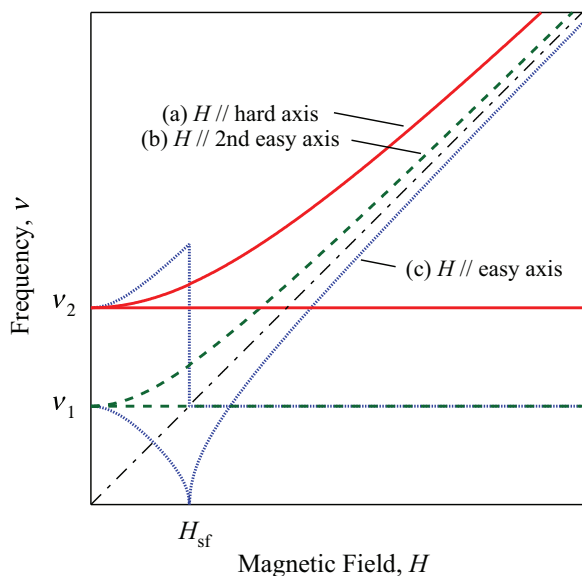


FIG. 7. (Color online) Resonance modes of a biaxial antiferromagnet at absolute zero. The red solid, green broken, and blue dotted curves are those for magnetic fields along the hard axis, the second-easy axis and the easy axis, respectively. The dashed-and-dotted line shows a paramagnetic resonance mode with $\omega/\gamma = H$. The zero-field gaps ν_1 and ν_2 are given by $2\pi\nu_1/\gamma = \sqrt{2H_E H_{A1}}$ and $2\pi\nu_2/\gamma = \sqrt{2H_E H_{A2}}$, respectively. The spin-flop field H_{sf} is given by $H_{sf} = \sqrt{2H_E H_{A1}}$.

Figure 7 shows a general resonance modes of a biaxial antiferromagnet possessing two magnetic sublattices. The red solid, green broken, and blue dotted curves correspond to the modes for magnetic fields along the hard axis, the second-easy axis and the easy axis, respectively. In our ESR experiments, the microwave frequency was fixed by using resonators and the signal was detected by sweeping the external magnetic field. Hence, the field-independent modes with constant resonance frequencies are undetectable. Furthermore, we ignored the easy-axis modes below the spin-flop field, H_{sf} , by assuming that the zero-field gaps, ν_1 and ν_2 in Fig. 7, are well below used microwave frequencies. Consequently, three resonance modes, which are indicated by (a)–(c) in Fig. 7, are expected to be relevant to the experimental data in the case of biaxial anisotropy. According to an analytical calculation,²⁴ the respective resonance conditions of these modes are given by

$$(\omega_a/\gamma)^2 = H^2 + 2H_E H_{A2}, \quad (2)$$

$$(\omega_b/\gamma)^2 = H^2 + 2H_E H_{A1}, \quad (3)$$

$$(\omega_c/\gamma)^2 = H^2 - 2H_E H_{A1}, \quad (4)$$

where H_{A1} and H_{A2} are the anisotropy fields related to the second-easy axis and the hard axis, respectively. The resonance modes in Eqs. (2) and (3) possess zero-field gaps given by $2\pi\nu_2/\gamma = \sqrt{2H_E H_{A2}}$ and $2\pi\nu_1/\gamma = \sqrt{2H_E H_{A1}}$, respectively, on the condition of $H_E \gg H_A$. On the other hand, the mode in Eq. (4) appears above the spin-flop field $H_{sf} = \sqrt{2H_E H_{A1}}$. In order to calculate a powder pattern spectrum, the resonance condition should be derived for a certain external field direction. Here, we define the direction of H by the polar angle θ and the azimuthal angle ϕ . θ is the

angle between the hard axis and the direction of H . ϕ is the angle between the easy axis and the direction of H projected to the plane involving both the easy axis and the second-easy axis. Based on Eqs. (2)–(4), the resonance condition under H with (θ, ϕ) direction is given by

$$\frac{(H \sin \theta \cos \phi)^2}{(\omega/\gamma)^2 + 2H_E H_{A1}} + \frac{(H \sin \theta \sin \phi)^2}{(\omega/\gamma)^2 - 2H_E H_{A1}} + \frac{(H \cos \theta)^2}{(\omega/\gamma)^2 - 2H_E H_{A2}} = 1. \quad (5)$$

This equation can be easily solved for H as a function of θ and ϕ to be

$$H(\theta, \phi) = \left[\frac{\sin^2 \theta \cos^2 \phi}{(\omega/\gamma)^2 + 2H_E H_{A1}} + \frac{\sin^2 \theta \sin^2 \phi}{(\omega/\gamma)^2 - 2H_E H_{A1}} + \frac{\cos^2 \theta}{(\omega/\gamma)^2 - 2H_E H_{A2}} \right]^{-\frac{1}{2}}. \quad (6)$$

The angular frequency ω is given by the microwave frequency ν ($=\omega/2\pi$) used in each measurement. Therefore, when the material parameters γ ($=g\mu_B/\hbar$), H_E , H_{A1} , and H_{A2} are given, we can obtain the resonance field at a certain direction of H to the crystal. Then, the AFMR powder pattern can be calculated by making a histogram of the resonance field with changing θ and ϕ over all the directions.

The exchange field H_E was evaluated from the magnetic susceptibility data. According to the molecular field theory, the Néel temperature T_N and the Weiss temperature Θ are given by

$$T_N = -2(z_1 J_1 - z_2 J_2) \frac{s(s+1)}{3k_B}, \quad (7)$$

$$\Theta = 2(z_1 J_1 + z_2 J_2) \frac{s(s+1)}{3k_B}, \quad (8)$$

with considering the exchange coupling constant also between the second NNs, J_2 . z_2 indicates the number of the second NNs. The values of z_1 and z_2 are eight and six, respectively, in the bcc lattice. The spin quantum number s is 1/2 according to the magnetic susceptibility data.¹⁵ By using the values of T_N and Θ for K_4^{3+} and $(K_3Rb)^{3+}$ clusters in sodalite reported in the previous work,¹⁵ J_1 and J_2 were evaluated. Then, we obtained the values of H_E by using Eq. (1). They are summarized in Table I. The residual parameters in Eq. (6) are γ ($=g\mu_B/\hbar$), H_{A1} and H_{A2} . They were treated as variable parameters in our simulation to fit the experimental data. We assumed isotropic g values for simplicity.

We also took into account the linewidth of each resonance mode mainly originating from relaxation processes with adopting two different methods as follows. The sodalite crystal has a cubic symmetry. Therefore we firstly assumed an isotropic width. The powder pattern histogram was convoluted by a Lorentzian function with a width of ΔH . Furthermore, as discussed in Ref. 10, we considered the inhomogeneous distribution of the zero-field gaps $\sqrt{2H_E H_{A1}}$ and $\sqrt{2H_E H_{A2}}$ and the spin-flop field H_{sf} because there might be some inhomogeneities in H_{A1} , H_{A2} , and H_E in the sample due to the imperfection of the alkali-metal loading and for other reasons. We assumed the distribution to be a Gaussian function. As an alternative possibility, we also tried to represent the spectra

TABLE I. Néel temperature T_N , Weiss temperature Θ , exchange coupling constants J_1 and J_2 , exchange field H_E and anisotropy fields H_{A1} and H_{A2} , and g value for Na_4^{3+} , K_4^{3+} , and $(\text{K}_3\text{Rb})^{3+}$ clusters in sodalite. H_{A1} , H_{A2} , and g were obtained from AFMR powder pattern analysis for the data at liquid helium temperature. The g values evaluated at room temperature (RT) are also shown.

	T_N (K)	Θ (K)	J_1/k_B (K)	J_2/k_B (K)	H_E (kOe)	H_{A1} (Oe)	H_{A2} (Oe)	g at liq. He T	g at RT
Na_4^{3+} ^a	48	-180 ± 5	-29	-22	1.7×10^3	0	1.7	2.00	2.001
K_4^{3+}	72 ± 1 ^b	-320 ± 22 ^b	-49	-41	2.9×10^3	0.26	1.3	2.05	1.999
$(\text{K}_3\text{Rb})^{3+}$	80 ± 1 ^b	-406 ± 41 ^b	-61	-54	3.6×10^3	0.48	0.95/0.96	2.06/2.07	1.994

^aFrom Refs. 10 and 11.

^bFrom Ref. 15.

by assuming anisotropic relaxation processes. Three different Lorentzian widths, ΔH_h , ΔH_{e1} , and ΔH_{e2} , were prepared for the hard-axis, the easy-axis, and the second-easy-axis modes, respectively. The (θ, ϕ) dependence of the linewidth was given by

$$\Delta H(\theta, \phi) = \Delta H_h \cos^2 \theta + \Delta H_{e1} \sin^2 \theta \cos^2 \phi + \Delta H_{e2} \sin^2 \theta \sin^2 \phi. \quad (9)$$

Then, the powder pattern histogram was convoluted by Lorentzian functions with the width of $\Delta H(\theta, \phi)$. In this case, we did not assume the inhomogeneous distribution of the zero-field gaps and the spin-flop field.

In accordance with the above methods, we tried to reproduce the observed AFMR signal at low temperatures at several frequencies. The red solid curves and the blue dashed curves in Fig. 6 show the simulation results of the AFMR powder pattern by assuming the isotropic and the anisotropic relaxation processes, respectively. In both cases, one can see that the spectral shapes are fairly well reproduced by the simulations at all the frequencies simultaneously, although some tail parts of the simulated spectra slightly deviate from the experimental data. It is hard to say which of the two models is better. In the isotropic width model, we used the Lorentzian linewidth of $\Delta H = 150$ Oe and the zero-field-gap distribution with a 10% standard deviation for both samples. These values are almost the same as those used in the simulation for Na_4^{3+} clusters.^{10,11} For K_4^{3+} clusters, the anisotropy fields $H_{A1} = 0.26$ Oe and $H_{A2} = 1.3$ Oe, and $g = 2.05$ were obtained. The zero-field gaps are calculated to be $\sqrt{2H_E H_{A1}} = 1.2$ kOe ($\nu_1 = 3.5$ GHz) and $\sqrt{2H_E H_{A2}} = 2.7$ kOe ($\nu_2 = 7.9$ GHz). For $(\text{K}_3\text{Rb})^{3+}$ clusters, the anisotropy fields $H_{A1} = 0.48$ Oe and $H_{A2} = 0.95$ Oe, and $g = 2.06$ were obtained. The zero-field gaps are calculated to be $\sqrt{2H_E H_{A1}} = 1.9$ kOe ($\nu_1 = 5.3$ GHz) and $\sqrt{2H_E H_{A2}} = 2.6$ kOe ($\nu_2 = 7.6$ GHz). The anisotropic width model also can reproduce the experimental data with using very similar values of the parameters. Slightly different values were used only for $(\text{K}_3\text{Rb})^{3+}$ clusters, namely, $H_{A2} = 0.96$ Oe and $g = 2.07$. However, it was necessary to use highly anisotropic linewidths, such as $\Delta H_h = 620$ Oe, $\Delta H_{e1} = 70$ Oe, and $\Delta H_{e2} = 270$ Oe for K_4^{3+} , and $\Delta H_h = 500$ Oe, $\Delta H_{e1} = 100$ Oe, and $\Delta H_{e2} = 220$ Oe for $(\text{K}_3\text{Rb})^{3+}$ in this model. The evaluated values of H_{A1} , H_{A2} , and g are summarized in Table I. They systematically vary depending on the species of alkali metal as described in the following section in detail.

We also applied the same simulation of the isotropic width model to the spectra taken at various temperatures below T_N . For a simplicity, we fixed the ratio H_{A1}/H_{A2} at the value

obtained at the lowest temperature. This treatment corresponds to an assumption of which the geometry of the magnetic anisotropy does not depend on the temperature. Then, the parameters of simulation are H_{A2} (or H_{A1}) and g value. The obtained values are plotted in Fig. 8. For the anisotropy field, $\sqrt{H_{A2}}$ is plotted. The g values above T_N were evaluated from the peak position of the spectra.

V. DISCUSSION

A. Magnetic anisotropy

As summarized in Table I, the magnetic anisotropy is extremely weak with the order of 1 Oe in all the samples

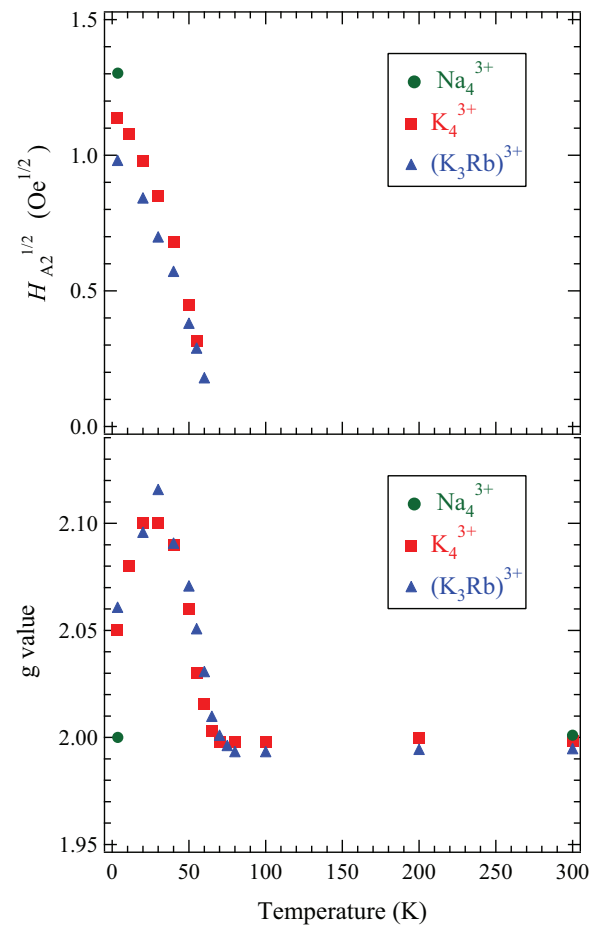


FIG. 8. (Color online) Temperature dependencies of anisotropy field and g value for Na_4^{3+} , K_4^{3+} and $(\text{K}_3\text{Rb})^{3+}$ clusters in sodalite. For the anisotropy field, $\sqrt{H_{A2}}$ is plotted. The data for Na_4^{3+} clusters are taken from Ref. 10.

whereas the exchange field is the order of 10^6 Oe. This result indicates that these materials are quite ideal Heisenberg-type antiferromagnets. This is one of the significant features of these materials. As mentioned above, each cluster has one unpaired electron, thus the magnetic moment with $s = 1/2$. Hence, the single-ion-type anisotropy is not necessary to take into account. For the classical dipolar magnetic field, the magnetic anisotropy cannot be produced as long as the cubic symmetry of sodalite crystal is maintained down to the liquid helium temperature. Therefore, it is reasonable that these materials possess almost no magnetic anisotropy. Although the observed anisotropies are extremely weak, they do not seem to have some extrinsic origins because they show a systematic change depending on the alkali element. When we change from Na to K and to K-Rb alloy clusters, H_{A1} (H_{A2}) systematically increases (decreases) as seen in Table I and also plotted in the upper panel in Fig. 9. Note that the condition with $H_{A1} = 0$ corresponds to an easy-plane-type anisotropy and that with $H_{A1} = H_{A2}$ to a uniaxial-type one. Therefore the systematic change in H_{A1} and H_{A2} from Na to K-Rb clusters seems to be a variation of the type of anisotropy from easy-plane to uniaxial. A possible origin of the weak magnetic anisotropy is a slight distortion of the crystal structure from its cubic symmetry. We calculated the dipolar field by assuming a lattice distortion from cubic symmetry to tetragonal one as an example. The results show that the lattice distortion with 0.2% change in the length of c -axis can produce the dipolar field of

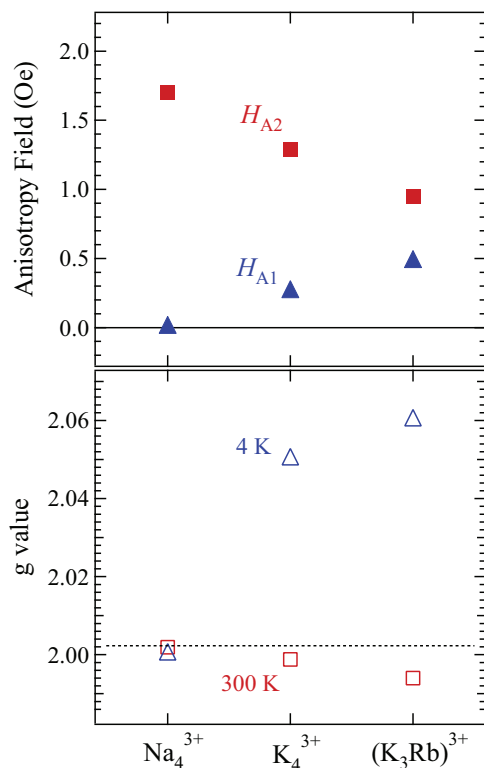


FIG. 9. (Color online) Alkali-element dependencies of anisotropy field and g value for Na_4^{3+} , K_4^{3+} and $(\text{K}_3\text{Rb})^{3+}$ clusters in sodalite. The data for Na_4^{3+} clusters are taken from Ref. 10. The horizontal dotted line in the lower panel indicates the free electron g value ($g_e = 2.0023$).

$\simeq 1$ Oe. According to the structural analysis by synchrotron radiation x-ray diffraction, the cubic symmetry is kept at the temperature down to 20 K.^{19,21} However, it is difficult to detect such a tiny distortion by using a typical setup of the diffractometer even if we use a synchrotron radiation light source, because the distortion gives less than 0.01 Å of the splitting of the Bragg peak in d spacing. Therefore the issue whether the alkali-element dependence of the magnetic anisotropy is caused by a tiny lattice distortions or not is still unclear. Very high-resolution x-ray diffraction measurements are required in order to clarify this issue.

As seen in the upper panel in Fig. 8, the anisotropy field decreases with increasing temperature and goes down to zero around T_N . If we assume the dipolar anisotropy, the relation $\sqrt{H_A H_E} \propto M(T)$ is expected. Here, $M(T)$ indicates the sublattice magnetization and is nothing other than the order parameter of antiferromagnet. In our analysis, the value of H_E was fixed and thus $\sqrt{H_A} \propto M(T)$ is expected. Therefore it is reasonable that the temperature dependence of $\sqrt{H_A}$ behaves like as the order parameter as seen in the upper panel in Fig. 8.

Generally, the hyperfine interaction between electronic and nuclear spins also can be an origin of weak magnetic anisotropy, which is known, for example, in cubic Mn^{2+} compounds such as KMnF_3 and RbMnF_3 .^{25–27} However, as discussed in the previous paper,¹⁰ the hyperfine field is too small to explain the observed anisotropy field in the case of Na_4^{3+} clusters in sodalite. Here, we calculate the hyperfine field in the case of K clusters in accordance with the same manner described in Ref. 10. Although the hyperfine coupling constant in K_4^{3+} cluster in sodalite is not known, an EPR study on almost the same K_4^{3+} clusters in the β cage in zeolite Y is reported.²⁸ From the EPR data, the hyperfine coupling constant is evaluated to be $A/g\mu_B = 16.4$ Oe. By using this value and the ^{39}K nuclear spin $I = 3/2$, the temperature T dependence of the hyperfine field is evaluated to be $H_A^{\text{hf}} = 0.090/T$ (Oe), which gives only $\simeq 0.02$ Oe at the liquid helium temperature. Hence, the hyperfine interaction cannot be the origin of the observed anisotropy also in the K_4^{3+} clusters.

B. g value

In the paramagnetic temperature region above T_N , the g values are temperature independent as seen in the lower panel in Fig. 8. It is clear that the heavier alkali-metal cluster has a smaller g value at room temperature as shown in Table I and also plotted in the lower panel in Fig. 9. The systematic decrease in g value in heavier alkali-metal has been commonly observed in other systems. For instance, bulk alkali metals Na, K, and Rb show g values of 2.0015, 1.9997, and 1.9984, respectively.²⁹ The ESR signal comes from the conduction electrons. The systematic increase in the g shift from the free electron g value ($g_e = 2.0023$) is well explained by the increase in spin-orbit interaction in the heavier alkali metals.^{30,31} Paramagnetic color centers (F centers) in alkali halides are also known to show a similar tendency in their g values. In the F center, an unpaired electron is trapped at a halogen vacancy and shared among the alkali cations which bound the vacancy. Thus the spin-orbit interaction of the alkali element affects the g value of the s -like electronic state in the F center. Indeed, the F -centers in NaCl, KCl and RbCl show the

g -values of 1.9978, 1.9958, and 1.9804, respectively.³² It was pointed out that the mixing the atomic p orbital on the alkali cation with the envelope s -like wave function is most important to explain quantitatively the g shift.³³ The situation in A_4^{3+} clusters in sodalite is quite similar to that in the F centers. The tail part of the s -like wave function of the cluster overlaps the alkali cations as schematically illustrated in Fig. 1(b). The systematic increase in the g shift can be well understood by the heavy atom effect of the spin-orbit interaction as described in F centers. As seen in Fig. 4, the EPR line is broader in the heavier alkali-metal clusters in the paramagnetic temperature region. The systematic increase in the linewidth also can be explained by the enhancement of spin-orbit interaction. In the exchange-narrowed Lorentzian spectra, the width is mainly determined by the relaxation rate. The spin-lattice relaxation is mediated by the spin-orbit coupling. Therefore the stronger spin-orbit coupling in the heavier alkali-metal cluster provides a shorter spin-lattice relaxation time, resulting in the broader EPR line.

In contrast to the paramagnetic temperature region, the g value shows an anomalous temperature dependence below T_N . The g value suddenly increases just below T_N and shows a peak at $\simeq 30$ K, and then decreases again at lower temperature both in the K_4^{3+} and $(K_3Rb)^{3+}$ clusters as seen in the lower panel in Fig. 8. The maximum g value is approximately 2.1 at 30 K. Generally speaking, this value is too large to be attributed to the true g value in alkali metals. In the case of ordinary weak anisotropy, the g value under the AFMR condition is basically same as the paramagnetic g value. This has been implicitly assumed also in the theoretical treatment of AFMR²⁴ and well explained the most of experimental results. Exceptional case was found in strongly anisotropic antiferromagnet such as $CoCl_2 \cdot 6H_2O$.³⁴ In this material, the slope of the AFMR modes at high-field limit deviates from that of the EPR line. This means that the g value in the AFM ordered state is much different from the paramagnetic g value. This phenomenon was well explained by taking into account an anisotropic exchange interaction of symmetric tensor form.³⁴ We tried to reproduce the experimental results in K_4^{3+} and $(K_3Rb)^{3+}$ clusters in sodalite by utilizing the AFMR modes with the anisotropic exchange interaction. However, we could not find any suitable parameters that satisfy both the very weak anisotropy and the large g shift simultaneously.

Large g shifts at low temperature have been often observed also in low-dimensional systems,^{35–37} spin glasses,^{38–40} and geometrically frustrated antiferromagnets such as kagomé^{41,42} or spinel⁴³ lattice systems. Some of them clearly show that the resonance field shifts to the lower-field side, namely, the higher- g value side, with lowering the temperature similar to the results in the present materials. In those systems, the development of short-range-magnetic ordering is believed to be the origin of large g shift at low temperature. In contrast to them, the long-range ordering and the three dimensionality were confirmed by neutron diffraction¹² and μ SR^{9,15} in the sodalite systems. However, one can notice that the magnetic frustration is immanent also in these systems. As shown in Table I, Θ has large negative values and the frustration index, $|\Theta|/T_N$, reaches approximately 5 in $(K_3Rb)^{3+}$ clusters, which is rather high in the nonfrustrated lattice.⁴⁴ This is originated

from the fact that the exchange coupling between the second NNs, J_2 , namely, the intrasublattice coupling, is also strongly antiferromagnetic. In the ordinary theories, AFMR modes are derived within a mean-field approximation, where rigid sublattice moments are assumed and the intrasublattice interaction, J_2 , is not considered. However, here we propose a possibility of that the frustration in the AFM exchange couplings affects the resonance field at the intermediate temperature region below T_N . Since this proposal is highly speculative, theoretical studies of AFMR beyond the mean-field theory considering the effect of the frustration are required in order to clarify the origin of the large g shift in alkali-metal clusters in sodalite.

VI. SUMMARY

We reported ESR studies of K_4^{3+} and $(K_3Rb)^{3+}$ clusters incorporated in powder specimens of aluminosilicate sodalite at several frequencies with varying temperature. We found sudden increases in the line width at temperatures below T_N in both materials. The spectral shapes at low temperatures were well reproduced by powder patterns of AFMR at all the frequencies by assuming a biaxial anisotropy. The evaluated anisotropy fields were extremely small as approximately 1 Oe, while the exchange coupling field was in the order of 10^6 Oe. This result clearly indicates that the systems are ideal Heisenberg-type antiferromagnets. This is a significant feature of the s -electron magnetic systems in the cubic lattice. Even in such a weak magnetic anisotropy, we found a systematic change depending on the species of alkali element. From Na_4^{3+} clusters to K_4^{3+} ones and to $(K_3Rb)^{3+}$ ones, the anisotropy type gradually changed from easy-plane type to biaxial one and closed to uniaxial one. The origins of the weak anisotropy and its change is not clarified, but the systematic change is indicative that the anisotropy is intrinsic. In the paramagnetic temperature region, a systematic decrease in g value as well as an increase in the spectral width was observed when we changed the alkali element from Na to K and to K-Rb alloy. This result was explained by the increase in the spin-orbit interaction and resultant enhancement of the spin-lattice relaxation in the heavier alkali atoms. On the other hand, below T_N , g value was found to show an anomalous temperature dependence accompanying with a large positive g shift. The origin of the large g shift is not known at the present stage. Some discussions were conducted by comparing with other materials such as geometrically frustrated antiferromagnets.

ACKNOWLEDGMENTS

We are grateful to Muneyuki Date (emeritus professor at Osaka University) for fruitful discussion. We also acknowledge to Keiji Itabashi, Masao Nakano and Hiroshi Ogawa (Tosoh Corporation) for the providing of high-quality sodalite crystals and to Shigeru Tamiya (Osaka University) for performing the chemical analysis. This work was supported by Grant-in-Aid for Scientific Research on Priority Areas (Nos. 19051009 and 19051010), for Scientific Research (A) (No. 242440590), and for Young Scientists (B) (No. 20710077), and also by Global COE Program (G10), from MEXT, Japan.

*nakano@phys.sci.osaka-u.ac.jp

- ¹Y. Nozue, T. Kodaira, and T. Goto, *Phys. Rev. Lett.* **68**, 3789 (1992); Y. Nozue, T. Kodaira, S. Ohwashi, T. Goto, and O. Terasaki, *Phys. Rev. B* **48**, 12253 (1993).
- ²T. Nakano and Y. Nozue, *J. Comput. Methods Sci. Engin.* **7**, 443 (2007).
- ³V. I. Srdanov, G. D. Stucky, E. Lippmaa, and G. Engelhardt, *Phys. Rev. Lett.* **80**, 2449 (1998).
- ⁴T. Nakano, K. Goto, I. Watanabe, F. L. Pratt, Y. Ikemoto, and Y. Nozue, *Physica B* **374-375**, 21 (2006).
- ⁵D. T. Hanh, T. Nakano, and Y. Nozue, *J. Phys. Chem. Solids* **71**, 677 (2010).
- ⁶T. C. Duan, T. Nakano, and Y. Nozue, *J. Magn. Magn. Mater.* **310**, 1013 (2007); *e-J. Surf. Sci. Nanotech.* **5**, 6 (2007).
- ⁷R. M. Barrer and J. F. Cole, *J. Phys. Chem. Solids* **29**, 1755 (1968).
- ⁸I. Heinmaa, S. Vija, and E. Lippmaa, *Chem. Phys. Lett.* **327**, 131 (2000).
- ⁹R. Scheuermann, E. Roduner, G. Engelhardt, H.-H. Klauss, and D. Herlach, *Phys. Rev. B* **66**, 144429 (2002).
- ¹⁰T. Nakano, T. Kashiwagi, A. Hanazawa, K. Watanabe, M. Hagiwara, and Y. Nozue, *J. Phys. Soc. Jpn.* **78**, 084723 (2009).
- ¹¹T. Kashiwagi, T. Nakano, A. Hanazawa, Y. Nozue, and M. Hagiwara, *J. Phys. Chem. Solids* **71**, 544 (2010).
- ¹²T. Nakano, M. Matsuura, A. Hanazawa, K. Hirota, and Y. Nozue, *Phys. Rev. Lett.* **109**, 167208 (2012).
- ¹³L. Damjanovic, G. D. Stucky, and V. I. Srdanov, *J. Serb. Chem. Soc.* **65**, 311 (2000).
- ¹⁴H. Tou, Y. Maniwa, K. Mizoguchi, L. Damjanovic, and V. I. Srdanov, *J. Magn. Magn. Mater.* **226-230**, 1098 (2001).
- ¹⁵T. Nakano, R. Suehiro, A. Hanazawa, K. Watanabe, I. Watanabe, A. Amato, F. L. Pratt, and Y. Nozue, *J. Phys. Soc. Jpn.* **79**, 073707 (2010).
- ¹⁶M. Igarashi, T. Nakano, A. Goto, K. Hashi, T. Shimizu, A. Hanazawa, and Y. Nozue, *J. Phys. Chem. Solids* **71**, 638 (2010).
- ¹⁷M. Igarashi, T. Nakano, A. Goto, K. Hashi, T. Shimizu, A. Hanazawa, and Y. Nozue, *J. Phys. Chem. Solids* **73**, 1534 (2012).
- ¹⁸O. F. Sankey, A. A. Demkov, and T. Lenosky, *Phys. Rev. B* **57**, 15129 (1998).
- ¹⁹G. K. H. Madsen, C. Gatti, B. B. Iversen, L. Damjanovic, G. D. Stucky, and V. I. Srdanov, *Phys. Rev. B* **59**, 12359 (1999).
- ²⁰R. Windiks and J. Sauer, *J. Chem. Phys.* **113**, 5466 (2000).
- ²¹G. K. H. Madsen, B. B. Iversen, P. Blaha, and K. Schwarz, *Phys. Rev. B* **64**, 195102 (2001).
- ²²K. Nakamura, T. Koretsune, and R. Arita, *Phys. Rev. B* **80**, 174420 (2009).
- ²³T. Moriya and H. Hasegawa, *J. Phys. Soc. Jpn.* **48**, 1490 (1980).
- ²⁴T. Nagamiya, *Prog. Theor. Phys.* **11**, 309 (1954).
- ²⁵A. J. Heeger, A. M. Portis, D. T. Teaney, and G. Witt, *Phys. Rev. Lett.* **7**, 307 (1961).
- ²⁶D. T. Teaney, M. J. Freiser, and R. W. H. Stevenson, *Phys. Rev. Lett.* **9**, 212 (1962).
- ²⁷W. J. Ince, *Phys. Rev.* **177**, 1005 (1969).
- ²⁸M. R. Harrison, P. P. Edwards, J. Klinowski, and J. M. Thomas, *J. Solid State Chem.* **54**, 330 (1984).
- ²⁹W. M. Walsh, L. W. Rupp, and P. H. Schmidt, *Phys. Rev. Lett.* **16**, 181 (1966).
- ³⁰Y. Yafet, *Phys. Rev.* **106**, 679 (1957).
- ³¹A. Bienenstock and H. Brooks, *Phys. Rev.* **136**, A784 (1964).
- ³²D. Schmid, *Phys. Status Solidi* **18**, 653 (1966).
- ³³A. H. Kahn and C. Kittel, *Phys. Rev.* **89**, 315 (1953).
- ³⁴M. Date, *J. Phys. Soc. Jpn.* **16**, 1337 (1961).
- ³⁵K. Nagata and Y. Tazuke, *J. Phys. Soc. Jpn.* **32**, 337 (1972).
- ³⁶K. Nagata, *J. Phys. Soc. Jpn.* **40**, 1209 (1976).
- ³⁷K. Oshima, K. Okuda, and M. Date, *J. Phys. Soc. Jpn.* **41**, 475 (1976).
- ³⁸S. Viticoli, D. Fiorani, M. Nogués, and J. L. Dormann, *Phys. Rev. B* **26**, 6085 (1982).
- ³⁹R. Troć, J. Janicki, A. Zygmunt, H. Drulis, and A. Niedźwiedź, *Physica B* **193**, 1 (1994).
- ⁴⁰G. Mozurkewich, J. H. Elliott, M. Hardiman, and R. Orbach, *Phys. Rev. B* **29**, 278 (1984).
- ⁴¹H. Ohta, M. Sumikawa, M. Motokawa, H. Kikuchi, and H. Nagasawa, *J. Phys. Soc. Jpn.* **65**, 848 (1996).
- ⁴²W. Zhang, H. Ohta, S. Okubo, M. Fujisawa, T. Sakurai, Y. Okamoto, H. Yoshida, and Z. Hiroi, *J. Phys. Soc. Jpn.* **79**, 023708 (2010).
- ⁴³S. Takano, T. Kaji, S. Okubo, H. Ohta, M. Yoshida, S. Kimura, R. Dziembaj, M. Molenda, C. Rudowicz, Y. Inagaki, and T. Asano, *J. Phys.: Condens. Matter* **19**, 145266 (2007).
- ⁴⁴J. E. Greedan, *J. Mater. Chem.* **11**, 37 (2001).